Near Infrared Absorption Imaging of Dense Scattering Media by Steady-State Diffusion Tomography

H. L. Graber[1], J. Chang[2,4], J. Lubowsky[1], R. Aronson[3], R. L. Barbour[1,2]
SUNY Health Science Center at Brooklyn, 450 Clarkson Ave., Brooklyn, NY, 11203,
Departments of [1]Physiology and Biophysics, and [2]Pathology.

Polytechnic University, 333 Jay Street, Brooklyn, NY, 11201,
[3]Physics and [4]Electrical Engineering Departments.

ABSTRACT

Results of experimental studies are presented based on steady-state optical tomographic measurements performed at 720 nm on tissue-like media having cylindrical geometry and a thickness equivalent to an uncompressed female breast. Experimental data were evaluated using a linear perturbation equation, previously described, derived from the transport equation. Results obtained demonstrate that high-resolution (<1 mm edge detection) images are recoverable of small-diameter objects buried at depths not visible from the surface.

INTRODUCTION

For many types of imaging problems, the upper limit of thickness or depth over which an image of a medium can be recovered is determined by the eventual loss of the straight-line component due to scattering. Beyond this, detection of only highly scattered signals is possible at the surface. Efforts to reconstruct images of media given this information requires solution of what is generally referred to as the *inverse 3-D scattering problem*. This problem is notoriously difficult on both theoretical and computational grounds. When electromagnetic sources are employed, solutions derived from the Helmholtz equation can be considered[1,2]. This approach requires, as input, measurement of the electric field at the boundary, *i.e.*, phase and amplitude measurements[3]. When the input source, however, is sufficiently randomized by the medium, the wave fronts arriving at the boundary are completely dephased, permitting measurement of only the power or intensity of the emerging energy. Under these conditions, formulations derived from the Helmholtz equation are unsuitable, and an alternative framework is required. The radiation transport equation is applicable for this problem, as it requires only intensity data as input[4], and it is the framework we have sought to apply.

In previous publications[5-10], we have described results of numerical experiments demonstrating the capability of reconstructing images of targets buried in isotropic scattering media based on solutions of a linear perturbation equation which is derived from the transport equation. Various numerical methods have been examined, including conjugate gradient descent, projection onto convex sets, and multi-grid and layer-stripping schemes[9, 11-14]. These results have shown that when only the backscattered field is considered, clearly recognizable images of the buried objects are recoverable even when the assumption of linearity, implicit in the perturbation equation, is violated by the presence of strongly absorbing objects. The ability to consider such targets will be important for many of the anticipated biomedical applications employing near infrared sources. Whereas body tissues are weakly absorbing at these frequencies[15], large diameter blood vessels will act to strongly attenuate penetrating photons. Although it seems likely that efforts to resolve fine structure in tissue will necessitate accounting for nonlinear effects caused by strongly attenuating structures[16], it is important to demonstrate, as a first step, the ability to resolve strongly absorbing targets buried in dense scattering media by evaluation of experimental data. This report presents such data evaluations using optical measurements performed at 720 nm with tissue-like media having a thickness equivalent to an uncompressed female breast.

MATERIALS AND METHODS

Light Source and Detector

A Coherent Innova 200 Ar-ion laser, operating in the multi-line mode, was used to pump a Coherent 599 dye laser operating at 720 nm using Pyridin 2 dye. Depending on experimental conditions and the location of the detector, the power of the dye laser beam was made to vary between 25 and 150 mW.

0-8194-1115-9/93/$6.00

A Hamamatsu C3140 cooled CCD camera, with a Micro-Nikkor 105 mm f/2.8 lens, was used as the detector. The camera was equipped with a Newport RG.610 color filter (50% transmission at 610 nm, >5 OD at 585 nm) to block light from the pump laser, and a polarizing filter to minimize detection of specularly reflected light. Depending on experimental conditions, the location of the detector, and the laser beam power, the lens aperture was varied between f11 and f32, and the duration of the light acquisitions was varied between 5 and 30 s.

Specimens

The tissue phantom consists of a Nalgene 2-liter graduated cylinder made of translucent plastic, 8.6 cm o.d. and 8 cm i.d. A 1.25 cm thick Plexiglas disk, containing holes that can serve as receptacles for rods of either 7 mm o.d. or 15 mm o.d., is cemented into the bottom of the cylinder. Similar disks with complementary holes fitted to the top of the cylinder allow it to hold rigidly as many as seven rods at once, all parallel to the cylinder axis. One of the seven available rod locations is at the cylinder axis; the other six are at the vertices of a regular hexagon, each located 2.25 cm from the axis. For the experiments whose results are presented here, the cylinder was filled to a height of 35 cm with a suspension of Intralipid® fat emulsion diluted with water. Three sets of measurements were performed, with suspensions containing 2%, 0.4%, and 0.08% lipid by volume. One rod was inserted into the cylinder as a heterogeneity. This was a hollow glass tube, 7 mm o.d. and 5 mm i.d., filled to a height of 36 cm with a diluted india ink solution (1 mL ink to 7.5 mL H_2O). See Figure 1 for sketch of phantom.

Independent measurements of the transport mean free pathlength (mfp) of the Intralipid® suspensions was carried out by Dr. R. R. Alfano at the Institute for Ultrafast Lasers and Spectroscopy at the City University of New York. These determinations involved measurements of the temporal profile of transmitted pulses from an ultrafast laser, and fitting the measured profiles with theoretical equations that give the shape as a function of the transport mfp and the absorption length[17]. These measurements show that the cylinder filled with Intralipid® at 2% concentration is approximately 200 transport mfp in diameter.

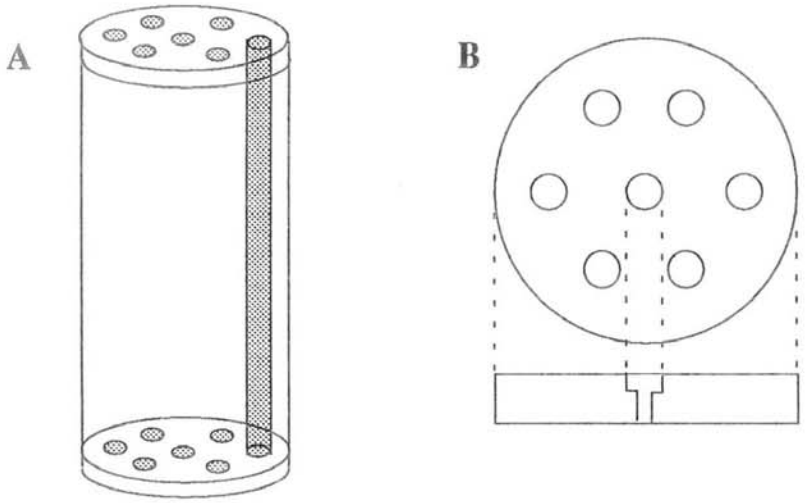

Figure 1 Panel A: Sketch of tissue phantom . Panel B: face- and edge-on views of bottom disk. The phantom holds up to seven rods at one time, and can take any combination 7 mm o.d. or 15 mm o.d. rods. Bottom disk has large-diameter holes drilled halfway through, and coaxial small-diameter holes drilled all the way through. Two complementary disks are stacked at the top. Topmost disk contains only holes for small-diameter rods; below it is a disk containing holes for shorter large-diameter rods.

Data Collection and Storage

The specimen was placed on a stand that is part of a custom-built optical scanner, which gives the operator manual control of the vertical positioning of the specimen and precise computerized control of its horizontal positioning (Daedal, Inc., 106041S linear positioning table). The stand is located directly above, but moves independently from, a rotary positioning table (Daedal, Inc., M20802-S). One end of a rigid boom is mounted to the rotary table. The camera is bolted to the other end, so that the distance from the rotation axis to the lens aperture is 66 cm (76 cm from axis to CCD); the operator has manual control of the vertical positioning of the camera. At this distance, the area of the cylinder surface patch seen by the camera is approx. 3.8 cm wide and 3.2 cm high. Because of the very large ratio of the distance between cylinder and camera to the diameter of the lens aperture, each pixel of the CCD acts as a highly collimated detector.

For the measurements presented here, the cylinder was positioned so that the laser beam impinged on it normally, at the mid-height level of the Intralipid® column, and the cylinder axis coincided with the axis of the rotary table. The camera was positioned so that the laser beam spot on the cylinder was vertically centered in the field of view when it was directly visible to the camera. A line drawn perpendicular to the CCD through its central pixel would strike the cylinder surface normally; this line is referred to as the "detector axis." Likewise, the line normal to the cylinder surface at the point where the laser beam enters is the "source axis." See Figure 2 for sketch of scanner.

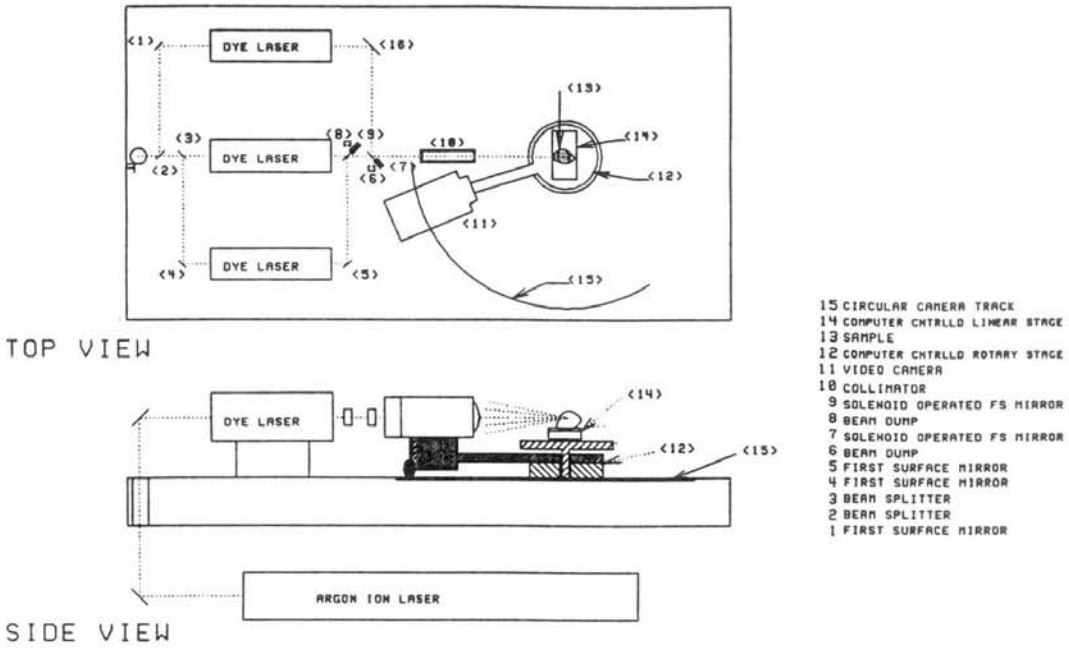

Figure 2 Sketch of experimental apparatus. Cylinder containing Intralipid® stands on translatory platform at one end of optical bench. The Hamamatsu 3140C CCD camera used as the detector revolves around the target at the end of a boom mounted to a rotating stage. The illuminating beam is produced by one of the three dye lasers on the optical bench, a Coherent 599 with Pyridin 2 dye. This, in turn, is pumped by a Coherent 200 Innova Ar-ion laser under the optical bench, whose beam is brought to the level of the dye laser by a periscopic device at the opposite end of the bench from the specimen. Data are digitized by and stored in a microcomputer

The first measurement set was taken with the camera positioned so that the angle between the source and detector axes, α, was 130°. The angle was then increased, in steps of 10°, until full transmission was measured (*i.e.*, angle between the source and detector axes was 180°). The camera then continued to revolve in the same direction about the cylinder in 10° steps, until α was 40°, for a total arc of 190°, with 20 measurement sets taken. As a consequence of the step size, most points on the cylinder surface within the field of view of the camera are seen in measurements made at six successive detector locations. This allows direct assessment of the direction-dependence of the light re-emitted at a point on the surface. See Figure 3 for sketch of measurement sweep pattern.

Data acquisition and storage were performed using the Hamamatsu Temporal Analyzer 4.0 application software, running on a Compaq Deskpro 286 computer. All images and profiles (*i.e.*, 1-D sections of images) placed in permanent storage were stored first as binary files, then subsequently converted to ASCII files for the data preprocessing and image reconstruction operations (see below).

At each of the twenty detector locations, the first measurement made was the distribution of light intensity re-emitted from the cylinder in the absence of the absorbing rod. The image of the cylinder surface obtained was stored in a file from which it could be continually retrieved into active display. The absorbing rod was then inserted successively into

each of the seven receptacles in the cylinder, and after each insertion a point-by-point software subtraction was performed between the light intensity detected from the cylinder-without-rod and from the cylinder-with-rod. During the entire set of eight measurements taken at each detector location, the camera aperture, detector gain, and acquisition time were all held constant. In addition, a portion of the dye laser beam was split off from the beam striking the target and sent to a power meter (Coherent Labmaster, with an LM-3 head). The power reading was continuously monitored during the course of the measurements, and only results in which the average power of the reference beam differed by < 1% between the two measurements were accepted.

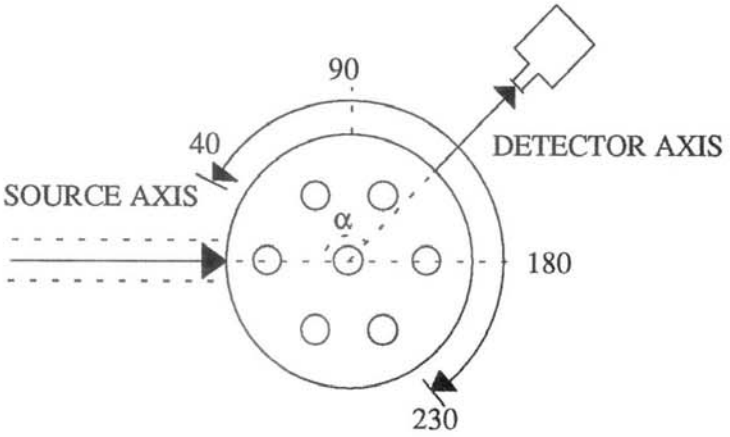

Figure 3 Sketch of experimental measurement procedure. End-on view of cylinder shows the arc (curved arrow) through which the camera was moved, in 10° steps, for a full set of measurements. This also illustrates the definition of source and detector axes, and angle α between them.

In each difference image thus obtained a horizontal window was selected, centered about the mid-point of the vertical dimension and approx. one-fifth the full height of the image. This window, 96 pixels high by 510 long, corresponds to a strip 6.4 mm high and 3.8 cm long on the cylinder surface. The resulting profile stored and used subsequently for image reconstruction consisted of 510 data points, each being the detected signal at one of the horizontal pixel locations, integrated between the vertical limits of the strip. Finally, the data from the cylinder-without-rod was recalled one more time, a dark-current subtraction performed, and a profile generated as just described. This was stored, to serve as reference data in the image reconstruction (see below).

Data Preprocessing

Every profile was smoothed by fitting it to polynomials of orders 1 through 4. The goodness of fit in each case was determined by examining the rate of increase of the correlation coefficient with each additional term added, and by visual inspection of the residuals plots. In most cases the fit of the quartic function was clearly superior to those of lower-order polynomials. In cases in which the impact of the absorbing rod on the intensity of light detected was small, however, it was often preferable to fit the profile with a lower-order polynomial. As the image reconstructions reported here employed weighting functions for only the case of detectors normal to the surface, only one data point from each smoothed profile was ultimately evaluated.

Image reconstruction

Perturbation Equation

As described in earlier publications[5-10], the general problem of reconstructing an image of dense scattering medium is nonlinear and usually intractable. This situation is greatly improved if the absorption properties of the target medium are known to deviate by only a small amount from those of a known reference medium. If this condition is met, the image reconstruction problem reduces to one of finding the solution to a system of linear equations:

$$\Delta \mathbf{I} = \mathbf{W} \Delta \Sigma_a \,. \tag{1}$$

In this system, each element of the vector $\Delta\Sigma_a$ is the difference between the macroscopic absorption cross-section (cm^{-1}) of the target medium and that of the reference medium, in a single volume element (voxel). Each row of the matrix **W** is a *weight function* that maps $\Delta\Sigma_a$ into an element of $\Delta\mathbf{I}$, the vector of detected intensity differences. Depending on the

definition of weight function used, ΔI may be either $I_0 - I$ or $(1 - I/I_0)$, where I_0 and I are, respectively, the intensity of light received by a given detector from the reference and target media.

Weight Function

The theoretical derivation of the weight functions used in the image reconstructions has been reported previously[6,16]. As was the case in these publications, those used here were calculated with the assumptions that the reference medium was homogeneous and light scattering was isotropic, and that only Σ_a of the target medium is different from that of the reference. Under these assumptions, and taking $\Delta\mathbf{I}$ to be the vector of absolute intensity differences, the mathematical formula for weight functions for CW measurements is:

$$w_{ij} = \frac{S_{0j} F_{0i} F_{ij}}{4\pi \Sigma_t^2 V_i}, \tag{2}$$

where w_{ij} is the element of matrix $\mathbf{W}$ corresponding to voxel i and source-detector pair j, S_{0j} is the source strength (photons-s^{-1}) for source-detector pair j, F_{0i} is the average number of collisions occurring in voxel i for every photon launched into the medium from the source, F_{ij} is the average number of collisions occurring in voxel i for every photon launched into the medium along the axis of the *detector*, Σ_t is the macroscopic total cross-section (cm^{-1}), and V_i is the volume of voxel i. If the elements of $\Delta\mathbf{I}$ are instead the relative intensity differences, it is necessary to include an additional factor of I_0 in the denominator in eq. 2.

For the weight functions used (see Results) in the image reconstructions, F_{0i} and F_{ij} were calculated by Monte Carlo simulations of photons propagating through a homogeneous cylindrical medium with an infinitely long axis. The simulation programs were written in the UNIX version of FORTRAN 77, and run on IBM RS6000 workstations of the CAT computer network at Syracuse University.

Iterative Reconstruction Algorithm

It is not practical to attempt direct solutions of eq. 1, because of the need for precise calibration of the detectors to obtain highly accurate absolute values of I_0 and I, because the matrix $\mathbf{W}$ can be expected to be ill-conditioned, and because the unavoidability of considering light propagation through 3-D volumes means most problems of interest will be underdetermined. As described in[6], the iterative backprojection reconstruction algorithm used here was designed to permit imaging studies to proceed even before fully adequate answers to these problems had been found. The mathematical description of this algorithm is[7]:

$$s_i^n = s_i^{n-1} + \frac{\sum_j w_{ij} \left[\left(\frac{\Delta I}{I_0} \right)_j - c_j^{n-1} \right]}{\sum_j w_{ij}}, \tag{3a}$$

$$c_j^n = \frac{\sum_i w_{ij} s_i^n}{\sum_i w_{ij}}, \tag{3b}$$

with $n \geq 1$, and $s_i^n = 0$ for all voxels, $c_j^0 = 0$ for all source-detector pairs. s_i^n is the estimate at iteration n of the image intensity in voxel i, c_j^n is the estimate at iteration n of the relative attenuation at source-detector pair j.

This algorithm was implemented in two distinct ways. The first is *non-progressive* reconstruction, in which all detector readings are evaluated simultaneously. The second, or *progressive* reconstruction, considers only readings for the smallest value of α initially, and sequentially incorporates data for successively larger α, after a preset number of iterations each time.

The reconstruction programs were run on the same computer system as the simulation programs, and written in the same programming language.

RESULTS

Raw Data

Examples of reflectance and transmittance data obtained in measurements about the phantom are shown in Figure 4. In these polar graphs the distance from the pole to the curves is proportional to the logarithm of the light intensity detected at each camera location. For this display, the data are normalized by dividing each intensity reading by the lowest value recorded in the set. The data show that the reflected intensity increases approximately 3 orders of magnitude in going from $\alpha = 180°$ to $\alpha = 40°$. Also evident is that whether the absorbing rod is at the axis of the cylinder or off-axis, the relative attenuation of light detected is small in most cases.

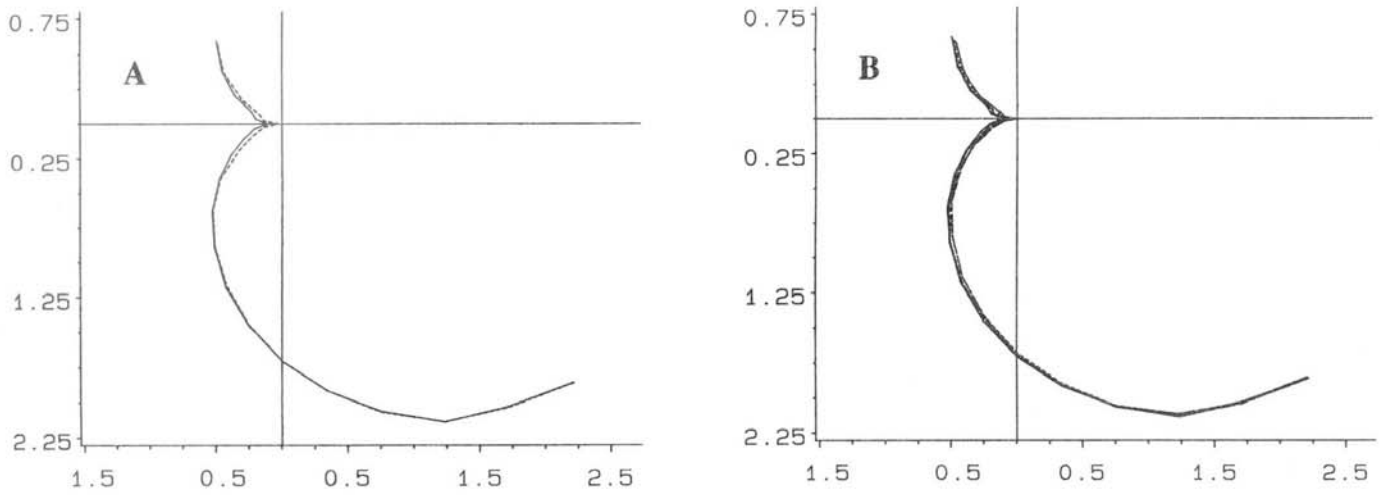

Figure 4 Raw data curves. Plane of figure is ⊥ cylinder axis, which intersects figure at the pole, (0,0). The source beam illuminates the medium from the right-hand side. The distance from the pole to a point on a curve is the common logarithm of the intensity reading, normalized by setting the smallest absolute intensity equal to 1.

Weight Functions

An example of the grid used in calculating the functions F_{0i} and F_{ij} is shown in Figure 5A. The particular case shown is that for an assumed cylinder diameter of 20 transport mfp. These functions also were calculated for diameters of 10, 40 and 100 transport mfp. Each cell in 5A is a 2-D section through a voxel with a depth of 1 transport mfp, and the volume of each is $\pi/4$ mfp^3.

Examples of 2-D sections through cylinder weight functions are shown in Figure 5B-5E. In each case the plane of section contains the source and detector axes, and is perpendicular to the cylinder axis. The contour lines are, therefore, sections through surfaces on which the weight has the values indicated in each panel. All of the weight functions illustrated were calculated for homogeneous media with isotropic scattering and $\Sigma_a = .01\Sigma_t$; they show the dependence of weight on α, on the diameter, and on the ratio of the refractive index of the cylinder to that of its surroundings.

Reconstructed Images, Absorber and Cylinder Coaxial

The particular weight functions used in an image reconstruction are based on values of the optical constants that are assumed to accurately represent the average values of the properties of the specimen medium. That is, the weights used will never be exactly correct for the medium being imaged. It will ultimately be necessary to incorporate procedures for

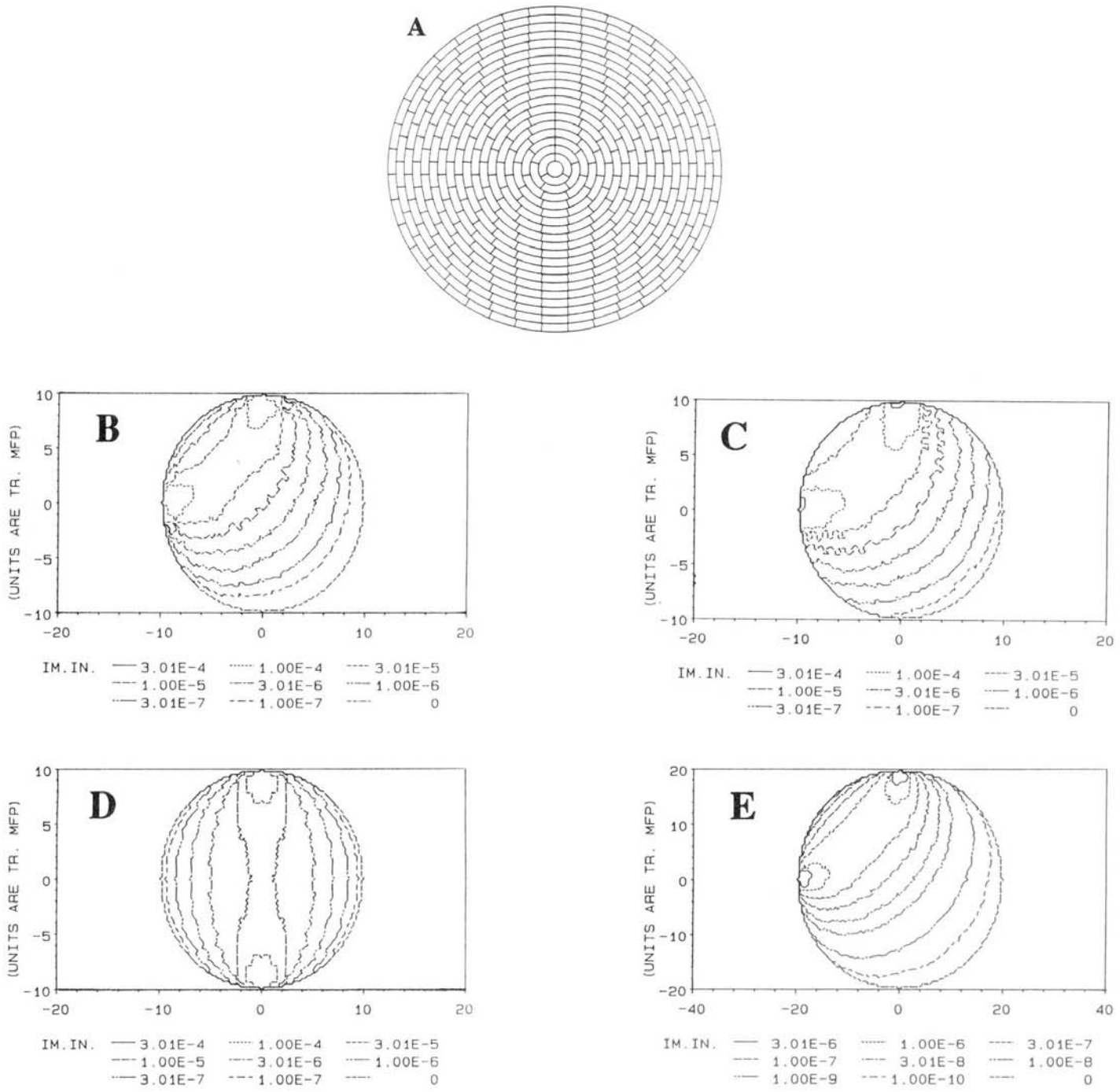

Figure 5 Panel A: voxel grid used for weight function calculation and image reconstruction. Although of varying shapes, all voxels have the same volume. 2-D sections through weight functions calculated for a homogeneous scattering medium in the shape of an infinitely long cylinder, ⊥ cylinder axis. Point collimated source enters, along normal to surface, at (x,y) = (0,10); point collimated detector receives light exiting normally at either (x,y) = (-10,0) (Panels A, C and E) or (x,y) = (0,-10) (Panel D). For every case shown, scattering is isotropic, there is no internal reflection at the boundary, and the macroscopic absorption cross-section is 1% of the total cross-section. The cylinder radius in transport mfp and the angle between source and detector axes are: Panels B and C, 10 and 90°; Panel D, 10 and 180°; Panel E, 20 and 90°. In B, D, and E, refractive index ratio in:outside cylinder is 1:1. In C, it is 1.33:1.

modifying the weights into the algorithm, to reflect both changed estimates of the mean values of the optical constants and their heterogeneity. It is of great value in the meantime to directly assess the sensitivity of the algorithm to quantitative errors in the weights. Consequently, weight functions were calculated, as described above (see Materials and Methods), for cylinders of four different diameters; the ratio of the largest diameter to the smallest is 10. The iterative reconstruction algorithm of eq.'s 3 was then applied to the experimental data along with each of the four sets of weight functions. The result obtained in the case of the absorber rod at the axis of the cylinder, 2% Intralipid® concentration, and an assumed cylinder diameter of 100 transport mfp, is shown in Figure 6. The graphed surface is plot of image intensity *vs.* position, and exhibits nearly perfect edge detection and the correct ratio of the diameter of the "spike" to that of the entire image domain. Other than a positivity constraint, this reconstruction did not incorporate any *a priori* information about the medium.

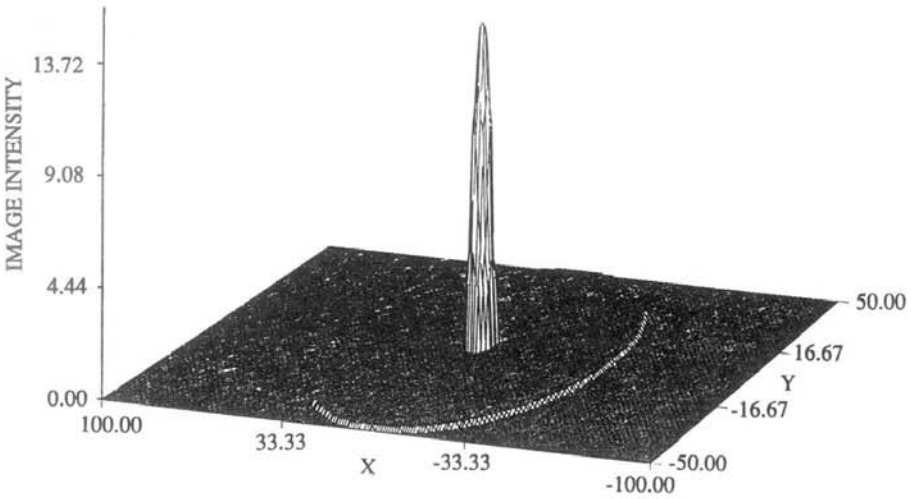

Figure 6 Image reconstructed from measurements about cylinder with Intralipid® concentration 2% and absorbing rod is on the cylinder axis. Weight functions were calculated for a cylindrical medium with diameter 100 transport mfp. See Table 1 for statistics on sharpness of edge and uniformity of image intensity under the peak.

Because of the radial symmetry of images such as that in Figure 6, it is economical to display only a 1-D slice through the result of reconstructions for the rod-on-axis case. Comparison of the result obtained using weight functions for different diameters and different Intralipid® concentrations is shown in Figure 7. It is seen that very good results are obtained for all three concentrations when the assumed diameter is 10 or 20 transport mfp. Together with the result in Figure 6, this indicates that accurate high-resolution images can be obtained even in cases in which there is considerable quantitative error in the weight functions used. In other reconstructions (not shown), the same detector readings were employed along with weight functions calculated for media exhibiting highly forward-directed scattering. These gave results that were qualitatively incorrect; the principal difference between the forward-directed scattering weights and the isotropic scattering weights is that the former typically exhibited the opposite gradient from the latter, increasing in magnitude with increasing depth. These results thus show that in cases the weight gradients lie in the correct directions the quality of the image is relatively insensitive to the precise properties selected for the reference medium.

It is seen that surface artifacts appear, along with suppression of the central "spike," for the case of 0.08% concentration and the assumed diameter 40 transport mfp. In addition, at each diameter, the edge detection and radius of the image are closest to being ideal for the most concentrated medium, and degrade as it becomes more dilute (see Table 1 for statistics on image intensity distributions). These observations are not unexpected, as the assumption that the voxel dimensions are greater than an equivalent isotropic step is most likely to be valid for the highest concentration of Intralipid®, and is increasingly violated as the concentration decreases. Further, the data set for the case of 0.08% concentration contained only 18 observations, with the smallest value of α being 60°. At $\alpha = 60°$, it was still the case that I was about 5% smaller than I_0. These results suggest that for the algorithm to accurately deduce that there is no absorption

near the surface, there must be values of ΔI close to 0 for detectors at α close to backscattering. Improved reconstructions would therefore be expected if data from detectors of more oblique reflectance had also been evaluated.

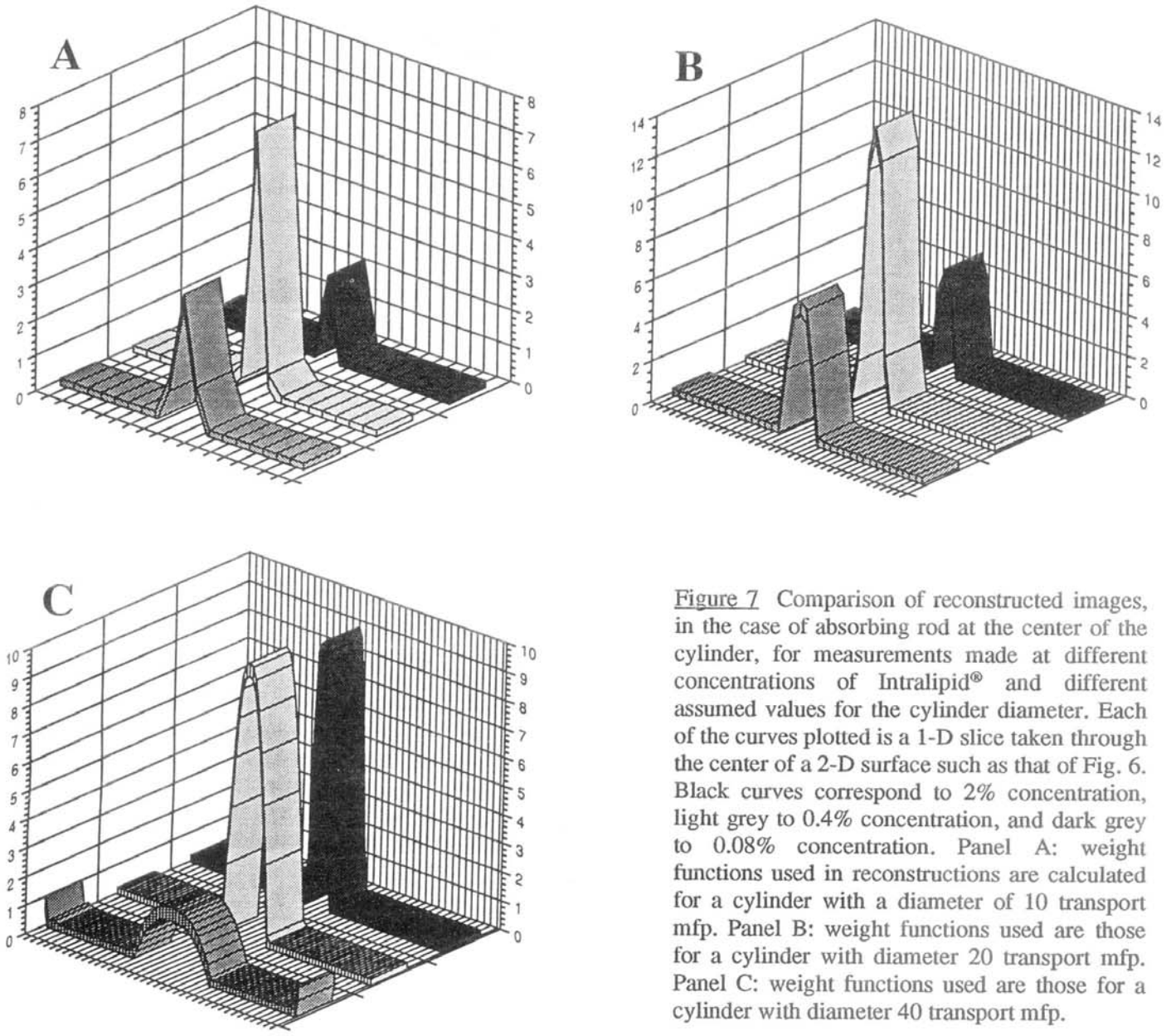

Figure 7 Comparison of reconstructed images, in the case of absorbing rod at the center of the cylinder, for measurements made at different concentrations of Intralipid® and different assumed values for the cylinder diameter. Each of the curves plotted is a 1-D slice taken through the center of a 2-D surface such as that of Fig. 6. Black curves correspond to 2% concentration, light grey to 0.4% concentration, and dark grey to 0.08% concentration. Panel A: weight functions used in reconstructions are calculated for a cylinder with a diameter of 10 transport mfp. Panel B: weight functions used are those for a cylinder with diameter 20 transport mfp. Panel C: weight functions used are those for a cylinder with diameter 40 transport mfp.

property\conc., diam.	2%,10	.4%,10	.08%,10	2%,20	.4%,20	.08%,20	2%,40	.4%,40	.08%,40*	2%,100
no. non-zero voxels	1	4	4	4	9	16	16	64	169	81
%age voxels non-zero	1.00	4.00	4.00	1.00	2.25	4.00	1.00	4.00	10.56	0.81
avg. image intensity	2.203	2.166	1.684	4.064	6.744	2.702	4.762	4.430	1.099	7.127
s. d. image intensity	0.000	2.891	1.068	0.442	4.903	2.502	3.000	3.139	0.638	3.549
r_{rms}	0.352	0.460	0.605	0.687	0.842	0.999	1.146	2.185	3.754	2.696
r_5	0.5	0.5	0.5	1.0	1.0	1.5	1.5	2.5	5.0	3.0
$r_1 - r_9$	0.0	0.0	0.5	0.5	1.0	0.5	1.5	2.0	3.5	3.0

Table 1 Measures of uniformity and edge detection of image of rod at cylinder axis. Ideally, all voxels in peak would have the same image intensity. First two rows give absolute number of voxels within the peak and the percentage of the total volume of the image with non-zero image intensity. Third and fourth lines contain the average value and standard deviation of the image intensity among the voxels in the peak; ideally the s. d. would be zero. Fifth row is the root mean squared distance of points in the peak from the axis, defined as $r_{rms} = \sqrt{\int s(\vec{r})|\vec{r}|^2 d\vec{r} \Big/ \int s(\vec{r}) d\vec{r}}$, where $s(\vec{r})$ is the image intensity as a function of position. Sixth row gives $r_{.5}$, an alternate measure of the peak's extent, defined as the distance at which the image intensity falls to one half its value at the axis. $r_{.9}$ and $r_{.1}$ are analogously defined as the distances at which it falls to 90% and 10%, respectively, of its maximum value. The "skin thickness," or difference between the latter two distances, as reported in the seventh row, is a measure of the sharpness of the detected edge. Calculations of values in column marked with (*) excluded the artifact in the four rings of voxels nearest the surface.

Reconstructions Assuming Straight Line Paths

As a control study, the measured relative ΔI were also processed by a reconstruction algorithm that assumed, as in x-ray CT, the photons traveled from source to detector along straight lines. The points at which the source and detector axes crossed the cylinder surface were joined by a straight line, and each voxel crossed by the line was assigned a weight of 1/N, where N is the total number of voxels crossed. All other voxels were assigned weights of zero. The reconstructed images obtained, for Intralipid® concentrations of 2%, 0.4%, and 0.08%, and for cylinder diameters of 10, 20, and 40 transport mfp, are shown in Figure 8. In these results there is frequently zero image intensity at the center; and although the intensity usually increases, as it should, in going from the surface to the center there is never good edge detection, the region of positive image intensity filling the entire volume of the cylinder. This shows that employing 3-D weight functions that are qualitatively correct is clearly superior to assuming straight-line paths.

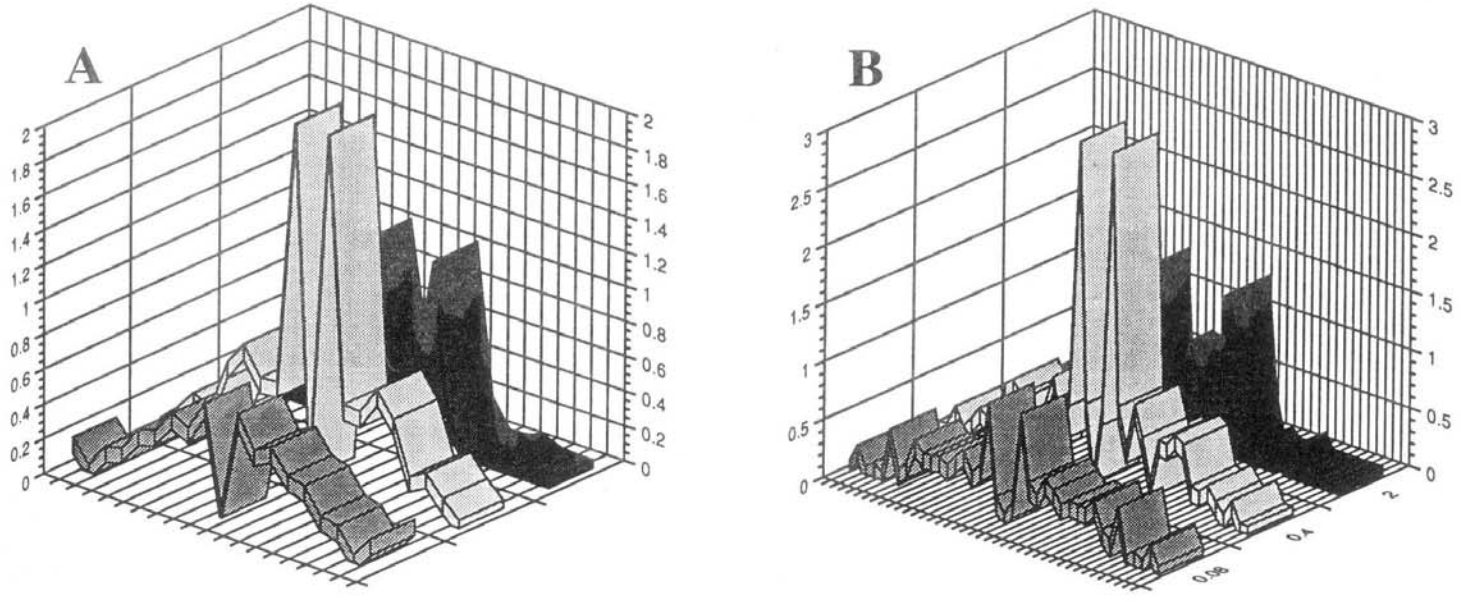

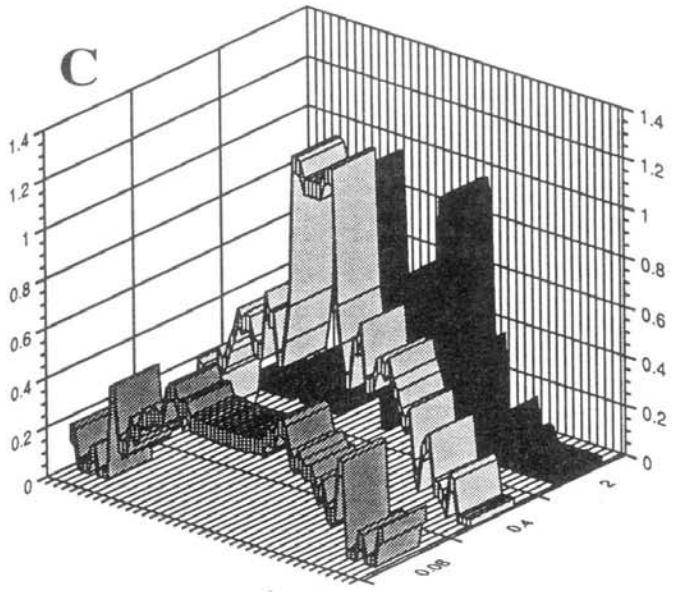

Figure 8 Comparison of reconstructed images, in the case of absorbing rod at the center of the cylinder, for measurements made at different concentrations of Intralipid®, different assumed values for the cylinder diameter, and assuming the path of light from source to detector is a straight line. Each of the curves plotted is a 1-D slice taken through the center of a 2-D surface, in the same manner as Fig. 7. Black curves correspond to 2% concentration, light grey to 0.4% concentration, and dark grey to 0.08% concentration. Panel A: cylinder diameter is 10 transport mfp. Panel B: cylinder diameter is 20 transport mfp. Panel C: cylinder diameter is 40 transport mfp.

Random Data "Images"

The results described above, in which accurate images were obtained with weight functions calculated for cylinders encompassing a ten-fold range of diameters as long as the weights decreased in moving from the surface to the axis, could suggest the apparent success of the reconstruction algorithm is only an artifact of the high degree of symmetry in the specimen and of the decrease in weight with increasing depth. According to this argument, a given value of ΔI could be produced by a heterogeneity in any voxel of the medium, but its magnitude must be inversely proportional to the weight; therefore, it is to be expected that the region of greatest image intensity will always be at the center, where the weight is lowest. If this objection were valid, it would be possible to replace the measured relative ΔI values with any set of numbers lying in the range of possible detector readings, and the algorithm would still produce a result similar to those shown in Figure 6 and Figure 7. As a control, image reconstructions were performed, with weight functions calculated for cylinders 10, 20, and 40 transport mfp in diameter, and the measured relative ΔI values replaced by a set of twenty numbers sampled from a random variable uniformly distributed between 0 and 1. The results, shown in Figure 9, varied significantly from one set of weight functions to the next, and in most cases the region of highest image intensity is far from the axis.

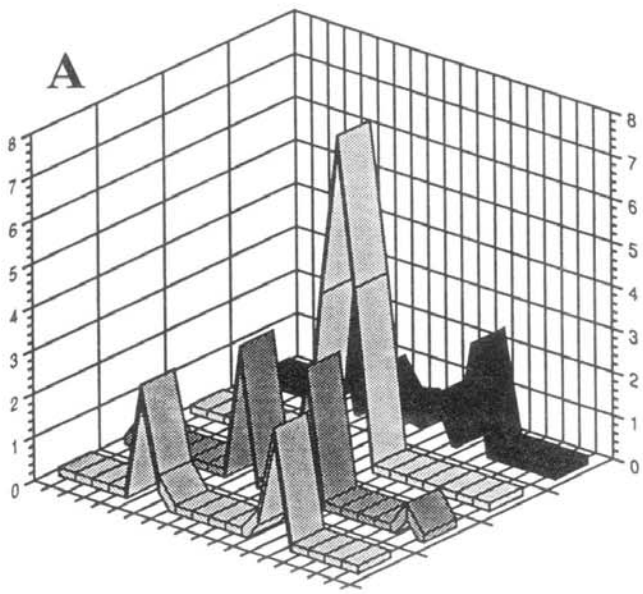

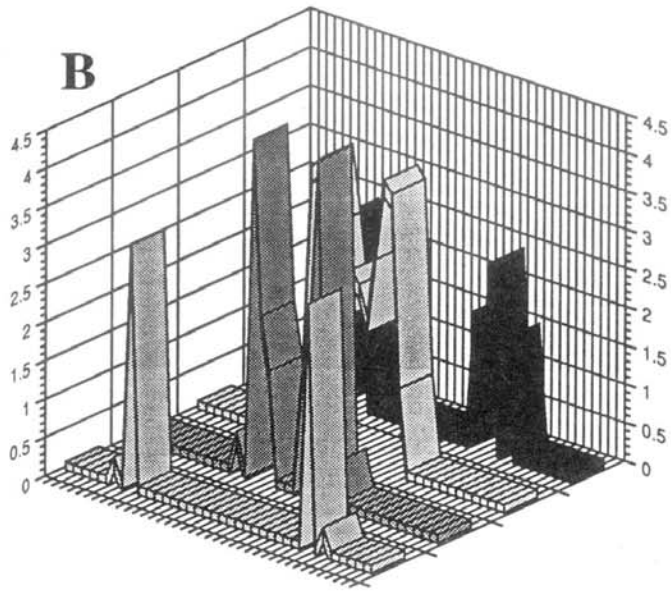

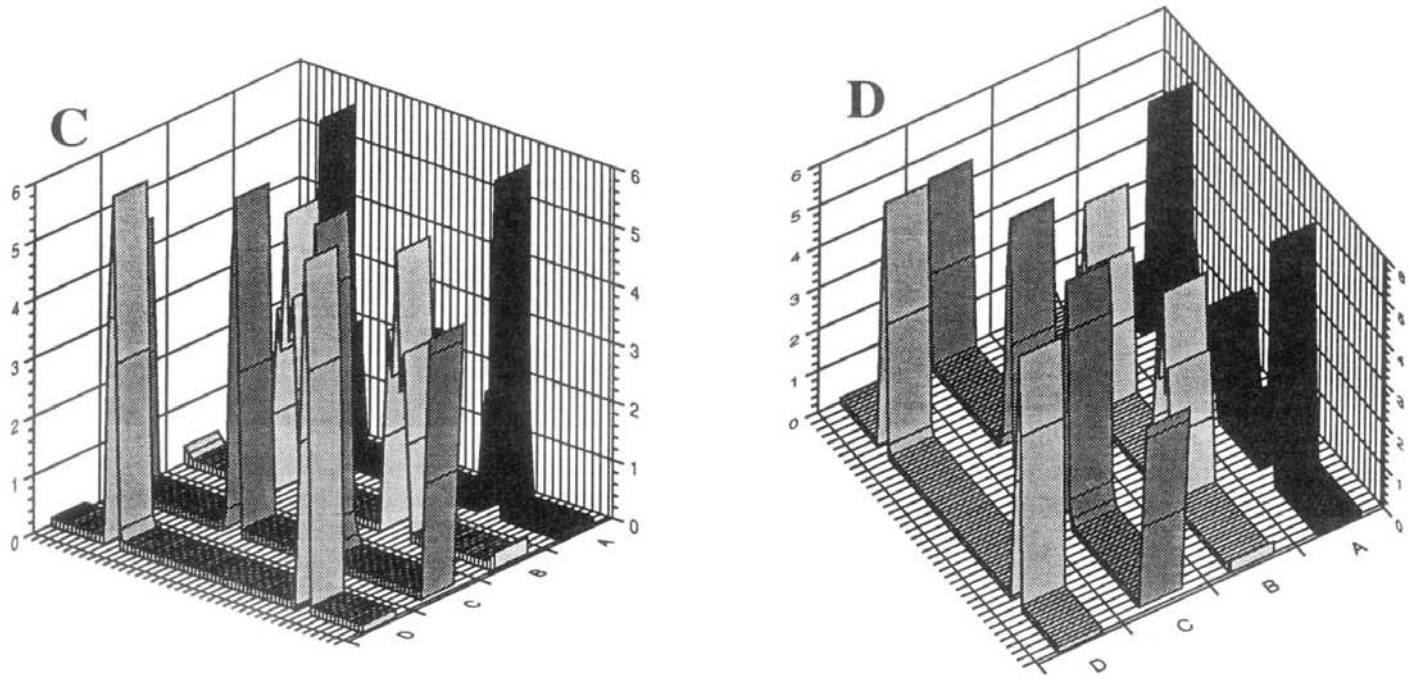

Figure 9 Comparison of reconstructed images, for different assumed values of the cylinder diameter, and substituting sets of random numbers for the measurement data. Each of the curves plotted is a 1-D slice taken through the center of a 2-D surface, in the same manner as Fig. 7. For the input data, four sets of numbers were created by sampling from a random variable uniformly distributed between 0 and 1, which was also the range of the normalized detector readings used for the reconstructions in Fig. 6 and Fig. 7. Panel A: weight functions used in reconstructions are calculated for a cylinder with a diameter of 10 transport mfp. Panel B: weight functions used are those for a cylinder with diameter 20 transport mfp. Panel C: weight functions used are those for a cylinder with diameter 40 transport mfp. Panel D: same curves as in Panel C, but rotated to reveal a feature in curve A that is obstructed in Panel C.

Convergence Rate

To quantify rates of convergence in different cases, all image reconstructions were allowed to proceed for ten thousand iterations, and permanent output files stored after every two hundred. Examples of surfaces showing image intensity *vs.* distance from axis *vs.* iteration number are shown in Figure 10. It is seen that the image intensity in a given voxel is a linear function of the number of iterations, with changes in slope occurring whenever the intensity in some voxels falls to zero. This pattern of convergence was seen in all reconstructions performed, and immediately suggests a way in which the rate of convergence could be increased. The program implementing the algorithm given by eq.'s 3 would be modified to detect extended periods of linearly changing image intensity, and to react by taking larger "steps" until the next change of slope.

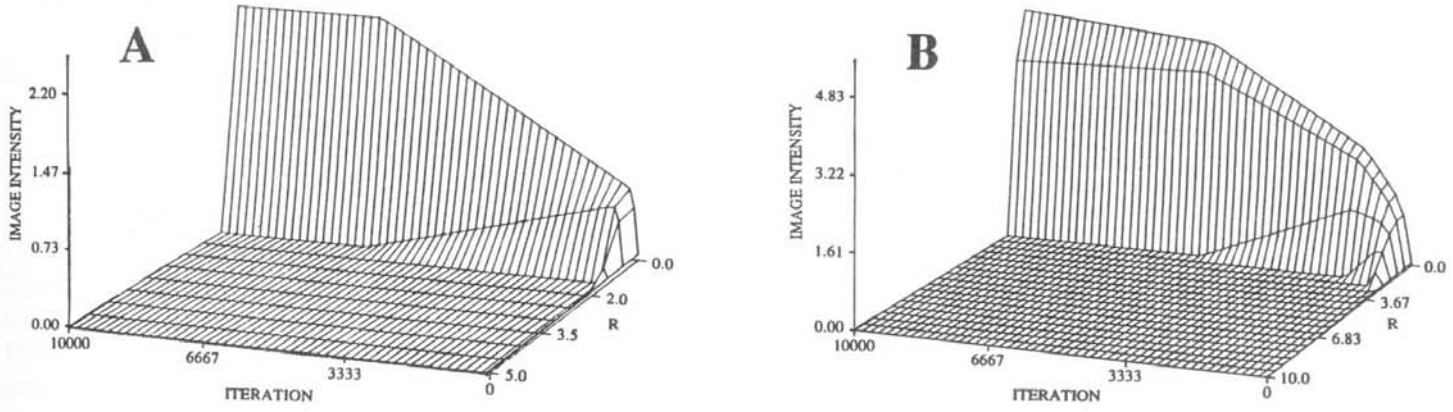

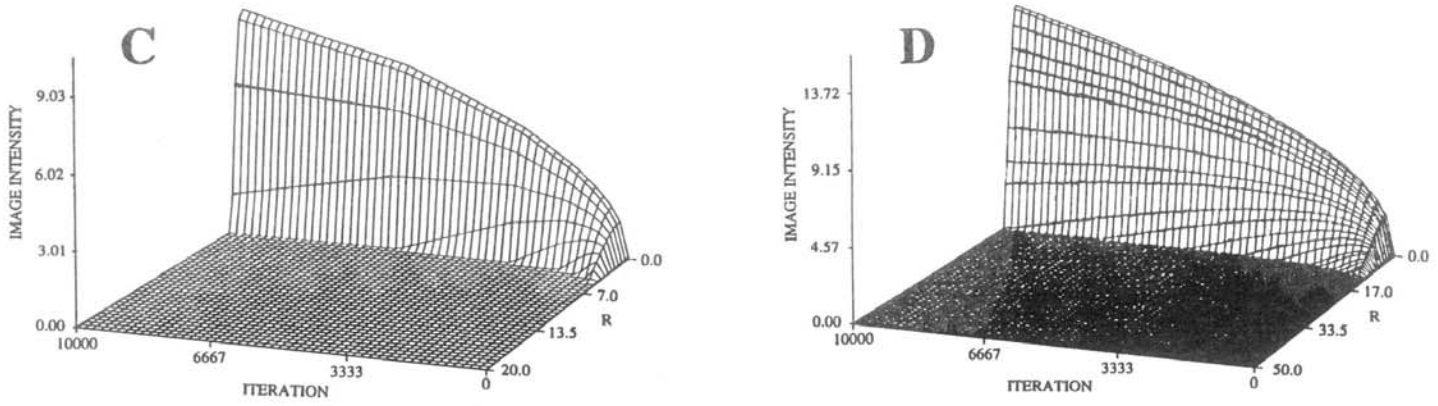

Figure 10 Image intensity *vs.* distance from axis *vs.* iteration number, for reconstructions based on measurements about cylinder with Intralipid® concentration of 2% and rod at cylinder axis. Panels A-D show results when the weight functions used were calculated for cylinders with diameters of, respectively, 10, 20, 40, and 100 transport mfp. Panel A shows that this reconstruction has converged completely at about 6200 iterations; all others were still changing when reconstruction stopped at ten thousand iterations. In every case, the image intensity at any distance is a linear function of the iteration number, with changes of slope occurring when the image intensity at some distance reaches zero.

Reconstructed Images, Rod off Cylinder Axis

As all the off-axis channels in the cylinder are the same distance from the axis, placing a single rod in each of them in succession is equivalent to rotating the source beam about the specimen. The six sets of measured relative ΔI were accordingly treated as a single data set for image reconstruction. The results for the case of 2% Intralipid® concentration are shown in Figure 11. Statistics relating to the image intensity distributions are given in Table 2.

Due to the voxel shapes (see Fig. 5A), it is not possible to accurately reproduce an object with a circular cross-section when it is not located at the center of the cylinder. Despite this limitation, the results obtained are highly compact with good edge detection, have the correct area and are very close to the expected location. Comparison of the images in 11C and 11D, finally, shows the definite improvement that can be achieved by implementing the algorithm in a progressive (11D) rather than non-progressive (11C) manner. This was accomplished only by considering the relative ΔI values in order of increasing α, without applying any constraints to the image intensities in superficial voxels.

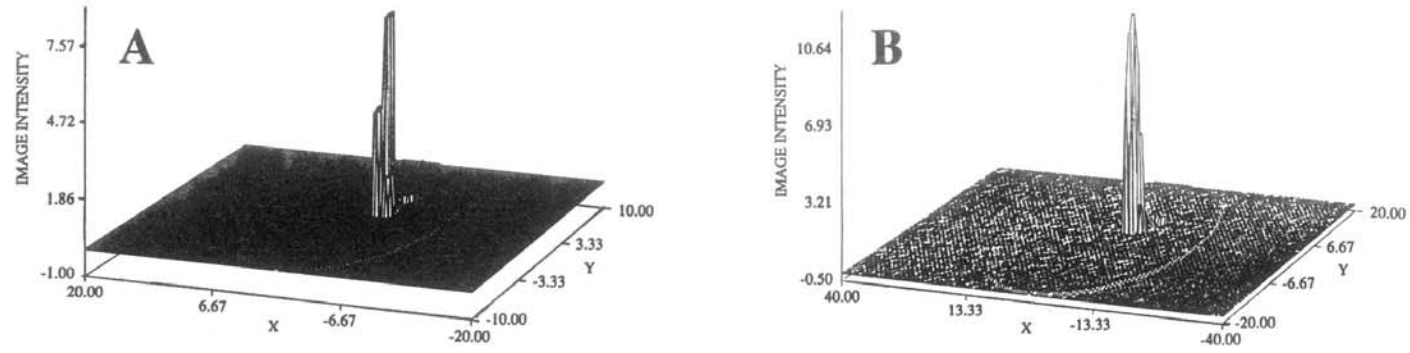

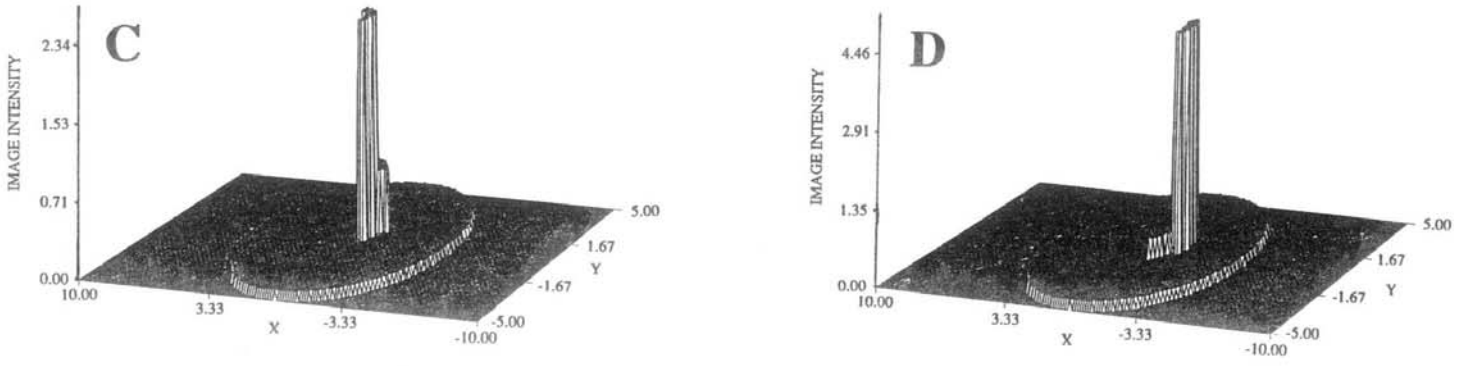

Figure 11 Reconstructed images for the case of absorbing rod off the cylinder axis, with Intralipid® concentration of 2%. Panel A: reconstruction using weight functions for a cylinder with 20 transport mfp diameter. Panel B: reconstruction using weight functions for a cylinder with 40 transport mfp diameter. Panel C: image obtained with weight functions for a cylinder of 10 transport mfp diameter and when reconstruction algorithm used is "non-progressive," *i.e.*, all detector readings are taken into consideration simultaneously from the start of the reconstruction. Panel D: image obtained with weight functions for a cylinder of 10 transport mfp diameter and when reconstruction algorithm is "progressive," *i.e.*, only measurements nearest backscattering (most acute angle between source and detector axes) are considered at first, followed by measurements approaching transmission (successively more obtuse angles between source and detector axes). This is effectively a layer-stripping algorithm, and yields a more accurate reconstruction.

property \ diam.	10	10 (prog.)	20	40
no. non - zero voxels	2	2	6	14
%age voxels non - zero	2	2	1.5	0.875
avg. image intensity	1.504	2.430	3.152	5.396
s. d. image intensity	0.835	2.034	2.435	3.298
R_{min}	0.5	1.0	2.0	3.0
R_{max}	1.5	2.0	4.5	7.0
R_{com}	0.745	1.639	2.932	4.778
α_{com}	50.4°	79.2°	70.5°	51.8°
r_{rms}	0.540	0.531	0.828	1.185

Table 2 Measures of uniformity and edge detection of image of rod off cylinder axis (CA). Ideally, all voxels in peak would have the same image intensity. First and second rows give absolute number of voxels with non-zero image intensity and the percentage of the total volume of the cylinder this peak occupies. Third and fourth rows give average value and standard deviation of image intensity among voxels in the peak. R_{min} and R_{max} are the smallest and largest distances, respectively, between a point of non-zero image intensity and the CA. R_{com} is the distance from the centroid of the peak to the CA. α_{com} is the angle between the ray joining the CA to the centroid and the source axis for the first of the six rod locations for which data were collected. Ideally, this would be about a 55° angle; in practice, the finite size and extensive curvature of the voxels mean the peak is correctly located if the angle is between 40° and 80° when the reconstruction uses an assumed diameter of 10 transport mfp, with the margin of error decreasing as the assumed diameter increases. r_{rms} is the root mean squared distance of points in the peak from the centroid. This is defined by the same formula as given in the legend to Table 1, but with $S(\vec{r})$ replaced by $S(\vec{r} - \vec{r}_{com})$.

DISCUSSION

Results described are the first to demonstrate the recovery of high-resolution 3-D tomographic images of dense scattering media having an equivalent thickness to that of an uncompressed female breast, based on steady-state near infrared measurements. The images shown here were reconstructed from measurements of media with high absorption contrast between the heterogeneity and the background. We chose this, in part, to assess the effects that large violations in the linearity assumption have on the resultant image. The errors seen in the reconstructed images are, however, quantitative not qualitative in nature. The only case in which clearly unsatisfactory results were obtained occurred when the weight

functions used had a qualitatively incorrect gradient, with the weight larger in voxels near the center than in those near the surface. This observation would suggest that estimates of weight functions having the correct direction of gradient may be sufficient for locating objects buried deeply in a highly scattering medium, at least for simply structured media.

REFERENCES

1. M. V. Klibanov, J. Malinsky, "Newton-Kantorovich method for three-dimensional potential inverse scattering problem and stability of the hyperbolic Cauchy problem with time-dependent data," Inverse Problems, vol. 7, pp. 577-596, 1991.

2. M. V. Klibanov, F. Santosa, "A computational quasi-reversibility method for Cauchy problems for Laplace's equation," SIAM J. Applied Mathematics, vol. 51, pp. 1653-1675, 1991.

3. A. Ishimaru, *Wave Propagation and Scattering in random Media*, chap. 2-6, Academic Press, Orlando, 1978.

4. *Ibid.*, chap. 7.

5. R. L. Barbour, J. Lubowsky, R. Aronson, "Method of imaging a random medium," U. S. Patent no. 5,137,355 (filed June 8, 1988; issued Aug. 11, 1992).

6. R. L. Barbour, H. Graber, R. Aronson, J. Lubowsky, "Model for 3-D optical imaging of tissue," proc. 10th Annual International Geoscience and Remote Sensing Symposium (IGARSS), vol. II, pp. 1395-1399, 1990.

7. R. L. Barbour, H. L. Graber, R. Aronson, J. Lubowsky, "Imaging of subsurface regions of random media by remote sensing," *Time-Resolved Spectroscopy and Imaging of Tissues*, SPIE vol. 1431, pp. 192-203, 1991.

8. R. L. Barbour, H. L. Graber, J. Lubowsky, R. Aronson, B. B. Das, K. M. Yoo, R. R. Alfano, "Imaging of diffusing media by a progressive iterative backprojection method using time-domain data," *Physiological Monitoring and Early Detection Diagnostic Methods*, SPIE vol. 1641, pp. 21-34, 1992.

9. Y. Wang, J. Chang, R. Aronson, R. L. Barbour, H. L. Graber, J. Lubowsky, "Imaging of scattering media by diffusion tomography: an iterative perturbation approach," *Physiological Monitoring and Early Detection Diagnostic Methods*, SPIE vol. 1641, pp. 58-71, 1992.

10. J. Chang, Y. Wang, R. Aronson, H. L. Graber, R. L. Barbour, "A layer-stripping approach for recovery of scattering media from time-resolved data," *Inverse Problems in Scattering and Imaging*, SPIE vol. 1767, pp. 384-395, 1992.

11. G. Strang, *Introduction to Applied Mathematics*, chap. 5, Wellesley-Cambridge Press, Wellesley, MA, 1986.

12. T. F. Budinger, G. T. Gullberg, R. H. Huesman, "Emission computed tomography," in *Image Reconstruction from Projections - Implementation and Applications*, G. T. Herman, ed., Springer-Verlag, New York, NY, 1979.

13. D. C. Youla, H. Webb, "Image restoration by the method of convex projections onto convex sets - Part I," IEEE Transactions on Medical Imaging, vol. 1, pp. 81-94, 1982.

14. T. S. Pan, A. E Yagle, "Numerical study of multigrid implementation of some iterative reconstruction algorithms," IEEE Transactions on Medical Imaging, vol. 10, pp. 572-588, 1991.

15. W.-F. Cheong, S. A. Prahl, A. J. Welch, "A review of the optical properties of biological tissues," IEEE J. Quantum Electronics, vol. 26, pp. 2166-2185, 1990.

16. H. L. Graber, J. Chang, R. Aronson, R. L. Barbour, "A perturbation model for imaging in dense scattering media: derivation and evaluation of imaging operators," SPIE Institute for Medical Optical Tomography, in press.

17. K. M. Yoo, F. Liu, R. R. Alfano, "When does the diffusion approximation fail to describe photon transport in random media?" Physical Review Letters, vol. 64, pp. 2647-2650, and vol. 65, p. 2210, 1990.